Liquid Crystals
Publication details, including instructions for authors and subscription information:
http://www.informaworld.com/smpp/title~content=t713926090

Computational modelling of nematic phase ordering by film and droplet growth over heterogeneous substrates

Benjamin Wincure[a]; Alejandro D. Rey[a]
[a] Department of Chemical Engineering and McGill Institute of Advanced Materials, McGill University, Montreal, Quebec, Canada H3A 2B2

To cite this Article Wincure, Benjamin and Rey, Alejandro D.(2007) 'Computational modelling of nematic phase ordering by film and droplet growth over heterogeneous substrates', Liquid Crystals, 34: 12, 1397 — 1413
To link to this Article: DOI: 10.1080/02678290701614657
URL: http://dx.doi.org/10.1080/02678290701614657

Liquid Crystals, Vol. 34, No. 12, December 2007, 1397–1413

Computational modelling of nematic phase ordering by film and droplet growth over heterogeneous substrates

BENJAMIN WINCURE and ALEJANDRO D. REY*

Department of Chemical Engineering and McGill Institute of Advanced Materials, McGill University, 3610 University Street, Montreal, Quebec, Canada H3A 2B2

(*Received 24 May 2007; accepted in revised form 7 August 2007*)

This paper presents a computational study of defect nucleation associated with the kinetics of the isotropic-to-nematic phase ordering transition over heterogeneous substrates, as it occurs in new liquid crystal biosensor devices, based on the Landau–de Gennes model for rod-like thermotropic nematic liquid crystals. Two regimes are identified due to interfacial tension inequalities: (i) nematic surface film nucleation and growth normal to the heterogeneous substrate, and (ii) nematic surface droplet nucleation and growth. The former, known as wetting regime, leads to interfacial defect shedding at the moving nematic-isotropic interface. The latter droplet regime, involves a moving contact line, and exhibits two texturing mechanisms that also lead to interfacial defect shedding: (a) small and large contact angles of drops spreading over a heterogeneous substrate, and (b) small drops with large curvature growing over homogeneous patches of the substrate. The numerical results are consistent with qualitative defect nucleation models based on the kinematics of the isotropic–nematic interface and the substrate–nematic–isotropic contact line. The results extend current understanding of phase ordering over heterogeneous substrates by elucidating generic defect nucleation processes at moving interfaces and moving contact lines.

1. Introduction

Many studies have reported on surface treatments that cause nematic liquid crystals to orient along a particular direction, known as the easy axis [1–5]. New research is now focusing on the methodical quantitative disruption of these treated surfaces, in the search for new sensor devices, such as biosensors where the addition of proteins and/or viruses to the treated surface causes deformations and defects in a thin nematic liquid-crystal film after an isotropic-to-nematic phase transition [6–20]. In these biosensors, the elastic deformations and defects in the thin nematic film create a macroscopic optical signature for the decorated surfaces when viewed with an optical polarizing microscope [21]. The optical signature is created from a non-equilibrium isotropic-to-nematic phase transition where the binding of biomolecules to the solid surface may influence (i) where the nematic phase nucleates on the surface, (ii) the transient growth of isolated nematic domains and (iii) the coarsening or relaxation of the nematic texture. Understanding the effect of the adsorbed bioparticles on these processes is crucial to the development of surface-based liquid crystal biosensors.

*Corresponding author. Email: alejandro.rey@mcgill.ca

Whereas there is a long tradition of investigating how deformation and defect densities change during coarsening [9, 21–26], much less effort has been directed to the early stages of the nematic growth process, which provides the initial conditions for coarsening. These initial conditions are important as they determine which nematic texture will be observed in the biosensor. When complicated decorated surfaces surround a thin liquid crystal film, we expect that slowly changing metastable states and multiple steady states are possible. This paper investigates an isotropic-to-nematic phase transition using a nucleation and growth model for the liquid crystal 5CB to explain how nematic deformations and defects occur under the influence of a propagating nematic-isotropic interface near a decorated surface. Once it is understood how the decorated surface and moving isotropic–nematic fronts interact to create the initial defects and deformations in the nematic phase, it should then be possible to better understand, predict, and manipulate the dynamics and structures of the observed thin film nematic textures in surface-based liquid crystal biosensors. This knowledge could then be applied to increase the reliability, precision and sensitivity of this new class of biosensor.

During the nematic–isotropic transition, nucleation corresponds to the first appearance of the nematic phase

Liquid Crystals
ISSN 0267-8292 print/ISSN 1366-5855 online © 2007 Taylor & Francis
http://www.tandf.co.uk/journals
DOI: 10.1080/02678290701614657

as a fluctuation in the original isotropic phase [27]. Typically surface nucleations occur before bulk nucleations [28, 29]. After nucleation occurs, the growth process involves the propagation of the stable nematic phase into the unstable isotropic phase [27]. After nucleation of the nematic phase occurs at a solid surface, two mechanisms interact to create texture in the nematic phase: (i) the heterogeneous substrate, and (ii) the moving nematic-isotropic interface, i.e. the propagating front. If these external forces have opposing orienting effects, then deformations and defects form in the growing nematic phase [30–32]. Deformations and defects generated during the nematic growth process may be pinned [9], slowly changing, or annihilated as the nematic texture expands [9, 21]. As isolated growing nematic regions come into contact with each other, some of the propagating nematic–isotropic fronts disappear, new fronts with discontinuous anchoring may be formed, and new defects and deformations can appear, for example, due to the Kibble mechanism [33]. Then the liquid crystal continues to modify its texture in response to the remaining external forces. Eventually, when the entire thin film has been converted to the nematic phase, i.e. the isotropic-nematic interfaces are no longer present, only the decorated surfaces remain to coarsen the nematic texture.

Experimental studies of isotropic-to-nematic transitions on different homogeneous or nearly homogeneous substrates indicate the presence of two possible nucleation and growth scenarios [34, 35]:

(i) Surface film condensation and growth (wetting regime): a nematic surface film arises through a surface phase transition that covers the entire substrate. This type of surface phase transition arises because of preferred mesogen/substrate interactions in the nematic phase, giving rise to wetting. If we neglect gradient elasticity, the interfacial tensions for the isotropic/substrate, γ_{is}, nematic/substrate, γ_{ns}, and nematic/isotropic, γ_{ni}, interfaces obey the following inequality:

$$\gamma_{is} > \gamma_{ns} + \gamma_{in}. \quad (1)$$

Once the nematic surface film forms through a surface phase transition, then the bulk phase transition emerges through the propagation of a phase ordering front travelling in the direction normal to the substrate. For biosensor applications, where the substrate is heterogeneous rather than homogeneous, we still expect that under wetting conditions a surface film may also arise. When the substrate is heterogeneous due to chemical composition or geometric heterogeneities, we can expect that even as equation (1) holds, the surface film will be heterogeneous and hence film growth will be heterogeneous, as summarized in figures 1 a and 1 b.

(ii) Surface droplet nucleation and growth (droplet regime): in this regime small nematic drops arise on the substrate and once they form the drops grow through the motion of the isotropic–nematic interface in the bulk and the motion of the contact line on the substrate. In this regime the interfacial tensions are expected to follow the inequality:

$$\gamma_{is} < \gamma_{ns} + \gamma_{in}. \quad (2)$$

This regime is illustrated in figures 2 a and 2 b.

In this paper, we are interested in establishing the nature of the texturing processes for both regimes (wetting and droplet) when the substrate is heterogeneous.

Previously, computer simulations of the isotropic-to-nematic phase transition based on the Landau–de Gennes model have provided basic understanding on the statics and dynamics of the process, including

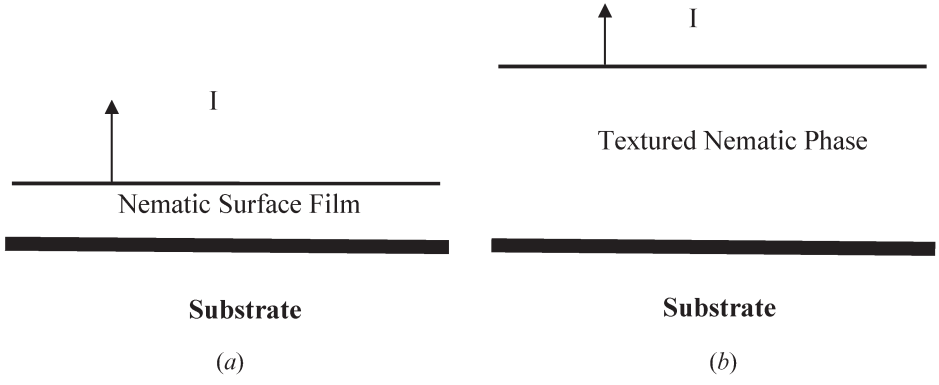

Figure 1. Schematic of phase ordering by surface film nucleation and growth. (a) Due to interfacial tension inequalities, a thin nematic wetting film arises next to the surface; this is known as a surface phase transition. (b) The film then grows normal to the substrate by the motion of the nematic-isotropic interface. If the substrate is heterogeneous the nematic phase will exhibit defects.

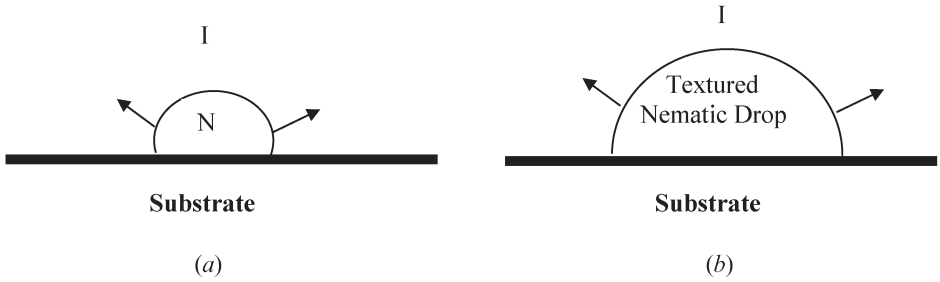

Figure 2. Schematic of the surface droplet nucleation regime. (a) Initially a drop in the form of a spherical cusp nucleates on the substrate. (b) The drop grows by the motion of the nematic (N)–isotropic (I) interface and also by the motion of the substrate–nematic–isotropic contact line. If the cusp has large curvature or if there are heterogeneities on the substrate the nematic phase will exhibit defects.

interfacial tension, spherulite shapes and the speeds of propagating fronts [36, 37]. Recently the theory was used in submicron geometries to shed light on new defect nucleation processes that occur in nematic spherulites due to large curvatures and heterogeneities along the nematic-isotropic interface [38]. In this paper we extend this work and use the Landau–de Gennes model to describe the isotropic-to-nematic phase transition in the presence of heterogeneous substrates, as in the biosensor device.

The specific objectives of this paper are:

1. To characterize texturing processes during the isotropic-to-nematic phase transition when the initial state of the transformation is a heterogeneous surface film that arises due to a surface phase transition, and corresponding to the wetting regime;
2. To characterize texturing processes during the isotropic-to-nematic phase transition when the initial state of the transformation is surface droplet nucleation that grows over a heterogeneous substrate;
3. To develop texture rules applicable to phase ordering over heterogeneous substrates for film and droplet growth.

The organization of this paper is as follows. Section 2 provides the theory and governing equations that we use to describe an isotropic-nematic phase transition near a heterogeneous surface. Section 3 shows the details of the computational modelling, including the initial conditions used to simulate nematic nucleation on the substrate and the time-dependent Dirichlet boundary conditions used to impose the desired contact line motion along the substrate. Section 4 discusses the results of the numerical simulations, which confirm that both surface melting and interfacial defect shedding will occur as nucleation and growth of the nematic phase occurs near heterogeneous surfaces. The numerical results indicate that nematic drops with large curvature growing over homogeneous patches of substrate, film growth over a heterogeneous substrate and large contact angle flat fronts that move across a heterogeneous substrate will each create near-surface disclinations of strength 1/2. Finally, section 5 presents the conclusions.

2. Theory and governing equations

To describe the kinetics of growth in a thermotropic isotropic-to-nematic phase transition requires (i) the spatio-temporal variation of an order parameter that distinguishes the two phases, (ii) the temperature, which affects the local driving force for the formation of the new nematic phase, and (iii) the viscoelastic material properties [27]. The appropriate order parameter is a symmetric, traceless second rank tensor $\mathbf{Q}$ referred to as the tensor order parameter, which can describe both the isotropic phase and the (average molecular) uniaxial and biaxial ordering of the nematic phase. In defect zones or at the isotropic-nematic interface, a full description taking into account the biaxiality of the system must be considered [39]. Minimizing the familiar Landau–de Gennes expression, which expresses the free energy of the system expanded in terms of the tensor order parameter $\mathbf{Q}$ and coefficients that are temperature-dependent or weakly temperature dependent, provides the spatial mean-field continuum theory predictions for nematic liquid crystal textures with elastic deformations and defects. The dynamical nature of the isotropic-nematic phase transition and subsequent texture formation is predicted from the time-dependent Ginzburg–Landau (TDGL) equation, a nonlinear reaction–diffusion equation solved without explicitly imposing the isotropic–nematic free boundary [27, 40]. This approach has previously been used to predict isotropic–nematic front velocities, interface width, interface biaxiality and texture formations in growing nematic liquid crystal droplets [36–39].

2.1. *Tensor order parameter Q*

Assuming that the liquid crystal molecules can be considered as uniaxial rods, the isotropic and nematic phases are described by a symmetric, traceless second rank tensor [1]:

$$\mathbf{Q}(\mathbf{r}, t) = \frac{1}{2}S(3\,\mathbf{nn} - \mathbf{I}) + \frac{1}{2}P(\mathbf{mm} - \mathbf{ll}), \tag{3}$$

where is $\mathbf{r}$ defines the location and t the time. The unit vectors $\mathbf{n}$, $\mathbf{m}$ and $\mathbf{l}$ form an orthogonal triad which characterizes the orientation of the phase where $\mathbf{n}$, the uniaxial director, is the direction of maximum orientational ordering [41] and $\mathbf{m}$ and $\mathbf{l}$ are biaxial directors, along which there may be a secondary preferred molecular ordering. $\mathbf{I}$ is the second rank unit tensor. Typically, the scalar quantities S (uniaxial scalar order parameter) and P (biaxial scalar order parameter) quantify the molecular alignment along the uniaxial director $\mathbf{n}$ and the first biaxial director $\mathbf{m}$, respectively. A physical interpretation of the tensor order parameter $\mathbf{Q}$ is obtained at a given time by diagonalization of the tensor, where the directors are given by the eigenvectors and the scalar order parameters by the associated eigenvalues [39]. The diagonalization of $\mathbf{Q}$ is shown below:

$$\mathbf{Q} = \begin{pmatrix} (-S-P)/2 & 0 & 0 \\ 0 & (-S+P)/2 & 0 \\ 0 & 0 & S \end{pmatrix}, \tag{4}$$

where

$$S = \mathbf{n}\bullet\mathbf{Q}\bullet\mathbf{n}, \tag{5a}$$

$$P = \mathbf{m}\bullet\mathbf{Q}\bullet\mathbf{m} - \mathbf{l}\bullet\mathbf{Q}\bullet\mathbf{l}. \tag{5b}$$

Three zero eigenvalues ($S=0$, $P=0$) indicate that the liquid phase is isotropic, i.e. no preferred molecular ordering. In the nematic phase, there is preferred molecular ordering, where the eigenvector associated with the largest absolute value eigenvalue corresponds to the direction of maximum orientational ordering, i.e. the uniaxial director. Nematic liquid crystal phase molecular ordering can be either uniaxial or biaxial, corresponding to two equal or three different nonzero eigenvalues, respectively. In the nematic phase, $S=1$ signifies that the liquid crystal molecules are aligning exactly with the uniaxial director, while a value of $S=-1/2$ indicates a planar degenerate ordering of the molecules, i.e. alignment along the plane perpendicular to the uniaxial director. With three different nonzero eigenvalues, the nematic liquid crystal phase is biaxial since the molecules on average have a primary and secondary preferred direction of ordering [42]. A full description of the possible combinations for S and P and their physical interpretation is given elsewhere [42].

2.2. *Landau–de Gennes theory of liquid crystal materials*

The Landau–de Gennes theory is a phenomenological model that expresses the free energy density difference between the nematic and isotropic bulk liquid crystal phases as a power series expansion of the tensor order parameter $\mathbf{Q}$ and its gradients $\nabla\mathbf{Q}$. This free energy density difference is expressed as [1, 43]:

$$\begin{aligned} f = {} & \frac{1}{2}a(T-T*)\mathrm{tr}(\mathbf{Q}^2) - \frac{1}{3}B\,\mathrm{tr}(\mathbf{Q}^3) + \frac{1}{4}C\left[\mathrm{tr}(\mathbf{Q}^2)\right]^2 \\ & + \frac{1}{2}L_1\partial_\alpha\mathbf{Q}_{\beta\gamma}\partial_\alpha\mathbf{Q}_{\beta\gamma} + \frac{1}{2}L_2\partial_\alpha\mathbf{Q}_{\alpha\gamma}\partial_\beta\mathbf{Q}_{\beta\gamma} \\ & + \frac{1}{2}L_3\mathbf{Q}_{\alpha\beta}\partial_\alpha\mathbf{Q}_{\gamma\delta}\partial_\beta\mathbf{Q}_{\gamma\delta}, \end{aligned} \tag{6}$$

where T is the temperature of the system, tr denotes the trace operation, T^* is the clearing point temperature below which the isotropic phase is no longer stable, and a, B, C, L_1, L_2 and L_3 are phenomenological material constants. For this investigation, the simulations are for 5CB (4-*n*-4′-pentyl-4-cyanobiphenyl), a thermotropic small molecule liquid crystal that is often used for the initial development of liquid crystal biosensors [6–7, 44] and other nanotechnologies [45–47]. For 5CB quenched to $T=25^\circ$C, the appropriate material parameter values are $T^*=34.2^\circ$C, $a=0.14\times10^6\,\mathrm{J\,m^{-3}\,K^{-1}}$, $B=1.8\times10^6\,\mathrm{J\,m^{-3}}$, $C=3.6\times10^6\,\mathrm{J\,m^{-3}}$, $L_1=3.0\times10^{-12}\,\mathrm{J\,m^{-1}}$, $L_2=3.0\times10^{-12}\,\mathrm{J\,m^{-1}}$ and $L_3=1.5\times10^{-12}\,\mathrm{J\,m^{-1}}$ [48–52]. The first, second and third terms in equation (6) are necessary to describe a first-order nematic–isotropic transition and the other three terms that include gradients of $\mathbf{Q}$ account for the unequal energies associated with splay, twist and bend elastic deformations in a liquid crystal such as 5CB [43, 51–52]. Uniaxial nematic 5CB at 25°C exhibits an experimentally determined equilibrium scalar order parameter of approximately $S_{eq}=0.58$ [52]. This experimental value, in addition to the measurements by Coles [48], were used to set the phenomenological parameters a, B and C.

2.3. *Time-dependent Ginzburg–Landau equation*

The time evolution of the symmetric and traceless tensor order parameter $\mathbf{Q}$ is governed by the time-dependent Ginzburg–Landau (TDGL) equation, which is a gradient flow model for a non-conserved order parameter such as $\mathbf{Q}$. That is, the rate of change in the tensor order parameter $\mathbf{Q}$ is proportional to the gradient of the free-energy functional [53]. This reaction-diffusion equation is [53, 54]:

$$\beta\frac{\partial\mathbf{Q}}{\partial t} = -\frac{\delta F}{\delta\mathbf{Q}} = \left[-\frac{\partial f}{\partial\mathbf{Q}} + \boldsymbol{\nabla}\bullet\frac{\partial f}{\partial\boldsymbol{\nabla}\mathbf{Q}}\right]^{[s]}, \tag{7}$$

where β represents a transport coefficient related to the rotational viscosity (γ_1) of the liquid crystal material, $\beta=(2/9)*(\gamma_1/S_{eq}^2)$, $\delta F/\delta \mathbf{Q}$ denotes the variational derivative operation, F is the free-energy functional, f is the free energy density and the superscript [s] denotes symmetric and traceless tensors. Since some operations on a symmetric traceless tensor do not yield a symmetric traceless result, we impose symmetry and tracelessness on all resulting tensors calculated from the right side of the TDGL equation:

$$\mathbf{H}^{[s]} = \frac{1}{2}[\mathbf{H} + \mathbf{trans}(\mathbf{H})] - \frac{1}{3}(\mathrm{tr}\ \mathbf{H})\mathbf{I}, \tag{8}$$

where $\mathbf{H}$ is the calculated tensor from the right side of the TDGL equation, $\mathbf{H}^{[s]}$ is the imposed symmetric traceless result, trans() is the transpose operation and $\mathbf{I}$ is the unit tensor. After imposing symmetry and tracelessness, the right side terms of the governing TDGL equation when combined with the Landau–de Gennes constitutive equation, in terms of $\mathbf{Q}$ and the gradients of $\mathbf{Q}$, are:

$$\begin{aligned}\frac{\partial f}{\partial \mathbf{Q}} &= a(T-T*)\mathbf{Q}_{ij} - B\left[\mathbf{Q}_{i\alpha}\mathbf{Q}_{\alpha j} - \frac{1}{3}\mathbf{Q}_{\beta\alpha}\mathbf{Q}_{\alpha\beta}\mathbf{I}_{ij}\right] \\ &\quad + C\mathbf{Q}_{\alpha\beta}\mathbf{Q}_{\beta\alpha}\mathbf{Q}_{ij} \\ &\quad + \frac{1}{2}L_3\left[\partial_i\mathbf{Q}_{\gamma\delta}\partial_i\mathbf{Q}_{\gamma\delta} - \frac{1}{3}\partial_\alpha\mathbf{Q}_{\gamma\delta}\partial_\alpha\mathbf{Q}_{\gamma\delta}\mathbf{I}_{ij}\right]\end{aligned} \tag{9}$$

and

$$\begin{aligned}\nabla\bullet\frac{\partial f}{\partial \nabla\mathbf{Q}} &= L_1\frac{\partial}{\partial \boldsymbol{x}_\alpha}\frac{\partial}{\partial \boldsymbol{x}_\alpha}\mathbf{Q}_{ij} + L_2\left[\frac{1}{2}\left(\frac{\partial}{\partial \boldsymbol{x}_i}\frac{\partial}{\partial \boldsymbol{x}_\alpha}\mathbf{Q}_{\alpha j}\right.\right. \\ &\quad \left.\left. + \frac{\partial}{\partial \boldsymbol{x}_j}\frac{\partial}{\partial \boldsymbol{x}_\alpha}\mathbf{Q}_{\alpha i}\right) - \frac{1}{3}\left(\frac{\partial}{\partial \boldsymbol{x}_\beta}\frac{\partial}{\partial \boldsymbol{x}_\alpha}\mathbf{Q}_{\alpha\beta}\right)\mathbf{I}_{ij}\right] \\ &\quad + L_3\left[\partial_\beta\mathbf{Q}_{\alpha\beta}\partial_\alpha\mathbf{Q}_{ij} + \mathbf{Q}_{\alpha\beta}\frac{\partial}{\partial \boldsymbol{x}_\beta}\frac{\partial}{\partial \boldsymbol{x}_\alpha}\mathbf{Q}_{ij}\right].\end{aligned} \tag{10}$$

For a quench to $T=25^\circ$C, the rotational viscosity (γ) of 5CB is assumed to be constant at $0.084\ \mathrm{N\,s\,m^{-2}}$ [55].

2.4. *Analytical results based on nematic–isotropic front dynamics and substrate–nematic–isotropic contact line dynamics*

As mentioned above, in the present paper we investigate two distinct phase ordering regimes: (i) nematic film growth normal to the heterogeneous substrate and (ii) droplet growth over a heterogeneous substrate by motion of the nematic–isotropic interface in the bulk and motion of the contact line over the substrate. In the first wetting regime there is no contact line and the phase ordering proceeds by the motion of the nematic-isotropic flat interface. In the second case the initial state corresponds to partial wetting and a substrate-nematic-isotropic contact line arises, where the substrate-nematic-isotropic contact line motion and the isotropic/nematic interface dynamics are coupled. Hence to characterize film and droplet growth over heterogeneous substrates, the dynamics of the bulk front and contact line need to be expressed in terms of viscoelastic bulk properties and substrate-mesogen properties.

The bulk motion of the nematic-isotropic interface is found by deriving the normal component of the interfacial force balance equation. It has been previously shown that the force balance equation at the moving nematic-isotropic interface is given by the sum of loads, capillary forces, and dissipation [36–38, 56–61]:

$$\beta_s w_s = \underbrace{\mathbf{L}\cdot\mathbf{k}}_{load} + \underbrace{(\nabla_s\cdot\mathbf{T}_s)\cdot\mathbf{k}}_{capillarity} + \underbrace{\beta\ \mathbf{Q}^s : \frac{d\mathbf{Q}^s}{dt}}_{dissipation} \tag{11}$$

where β_s is the interfacial viscosity, w_s is the normal nematic–isotropic interface velocity, $\mathbf{L}$ is the net stress loading at the transverse interface boundary, $\mathbf{k}$ is the nematic–isotropic interface unit normal, ∇_s is the interfacial gradient tensor, $\mathbf{T}_s$ is the interface stress tensor, β is the viscosity, $\mathbf{Q}^s$ is the interface tensor order parameter and t is time. The load $\mathbf{L}\cdot\mathbf{k}=L_h+L_g$ has homogeneous and gradient components:

$$\begin{aligned}L_h &= [f_h h]_{\lambda=\Delta_I} - [f_h h]_{\lambda=\Delta_N} = \Delta f_h, \\ L_g &= -\left[\mathrm{f_g} - \mathbf{kk} : \frac{\partial f_g}{\partial \nabla\mathbf{Q}} : (\nabla\mathbf{Q})^{\mathrm{T}} h\right]_{\lambda=\Delta_I}\end{aligned} \tag{12}$$

where L_h is the homogeneous free energy difference between the isotropic and nematic phases, and L_g is the load due to gradient contributions (where contributions from the isotropic phase are negligible), h is the area magnification factor, λ is the normal coordinate, $\lambda=\Delta_I$ is the location of the isotropic region, $\lambda=\Delta_N$ is the location of the nematic region, and superscript T represents the transpose operation. For the nematic–isotropic phase transition, the most significant contribution to the load is the free energy difference between the isotropic phase and the nematic phase. For $T<T^*$, this difference is positive and the load drives the front that replaces the unstable isotropic phase with the stable nematic phase. On the other hand the capillary effect $(\nabla_s\cdot\mathbf{T}_s)\cdot\mathbf{k}$ can be driving or resisting the front, since it is directed along the centre of curvature. For the nematic–isotropic interface, the capillary pressure in equation (11) is [37, 38]:

$$(\nabla_s\cdot\mathbf{T}_s)\cdot\mathbf{k} = \left(\nabla_s\cdot\int_{\Delta_N}^{\Delta_I}((1-2\lambda H)\mathbf{I}_s + \lambda\mathbf{b})\cdot\mathbf{T}_b\, d\lambda\right)\cdot\mathbf{k}, \tag{13}$$

where the bulk stress tensor is given by [37, 38]:

$$\mathbf{T}_b = \left(f_h + f_g\right)\mathbf{I} - \mathbf{kk} : \frac{\partial f_g}{\partial \nabla \mathbf{Q}} : (\nabla \mathbf{Q})^T. \tag{14}$$

For nematic drops growing in an unstable isotropic phase the capillary forces resist the growth [37, 38]. Furthermore, the presence of tangential gradients of $\mathbf{Q}$ introduces significant capillary forces that locally slow down the front and lead to the formation of cusps, which then cause instability and defect shedding [37, 38]. Dissipation, which occurs for a transient surface tensor order parameter, vanishes for a steady surface tensor order parameter.

Likewise the dynamics of the substrate–nematic–isotropic contact line is found by deriving the normal component of the force balance equation acting on the line. The exact and lengthy derivation will be given in a future publication; in this paper we do not use this equation except for the classification of different regimes. Based on previous work [62–65] and in correspondence to the interfacial kinematic equation (12) we find that the normal velocity of the contact line w_ℓ is:

$$\beta_\ell w_\ell = \underbrace{\left(\oint_{\text{jun}} (\mathbf{k}\bullet\mathbf{T}_b)\mathrm{d}\ell + \sum_{\text{jun}} v\bullet\mathbf{T}_s\right)\bullet\mathbf{p}}_{load} + \underbrace{(\nabla_\ell\bullet\mathbf{T}_\ell)\bullet\mathbf{p}}_{line\ \text{tension}} + \underbrace{\left(\eta\,\mathbf{Q}^\ell : \frac{d\mathbf{Q}^\ell}{dt}\right)\bullet\mathbf{p}}_{dissipation}, \tag{15}$$

where β_ℓ is a line viscosity, $\mathbf{T}_b$ is the bulk stress tensor, $\mathbf{v}$ is the tangent unit vector along each interface and perpendicular to the contact line, $\mathbf{p}$ is the normal to the principal normal to the contact line, η is a viscosity, $\mathbf{Q}^\ell$ is the tensor order parameter at the contact line, and jun represents the junction at which the three phases meet. The bulk force appearing in the load term in equation (15), given in terms of the junction integral is defined as:

$$\oint_{\text{jun}} (\mathbf{k}\bullet\mathbf{T}_b)\mathrm{d}\ell = \lim_{\delta\to 0}\sum_{\text{i}}\int_{D_\delta^{(i)}} \left(\mathbf{k}\bullet\mathbf{T}_b^{(i)}\right)\mathrm{d}\ell; \tag{16}$$

i = isotropic, nematic, substrate

where $\mathbf{k}$ is the unit normal to the circular integration domain D_δ, and the limit $\lim_{\delta\to 0}$ signifies that the junction integral is the net force at the contact line due to bulk elasticity. In general, this junction integral force $\oint_{\text{jun}} (\mathbf{k}\bullet\mathbf{T}_b)\mathrm{d}\ell$ acts to expand the contact line and remove $\mathbf{Q}$-gradients. The junction sum appearing in the load term in equation (15) is:

$$\sum_{\text{jun}} \nu\bullet\mathbf{T}_s = \lim_{\delta\to 0}\sum_{\text{i, j}}\left(\nu^{(i,j)}\bullet\mathbf{T}_s^{(i,j)}\right) \Big|_{e_\delta^{(i,j)}} = \nu^{(1,2)}\bullet\mathbf{T}_s^{(1,2)} + \nu^{(3,1)}\bullet\mathbf{T}_s^{(3,1)} + \nu^{(2,3)}\bullet\mathbf{T}_s^{(2,3)}\Big|_{C^{tl}}, \tag{17}$$

which is a force that acts on the contact line due to the three interfacial tensions. Here $\mathbf{v}^{(i,j)}$ is the unit normal to the interface and tangential to the (i, j) interface, where in the present case: i, j=isotropic, nematic, substrate. For simple fluids the surface stress tensors $\mathbf{T}_s^{(i,j)}$ are given by:

$$\mathbf{T}_s^{(i,j)} = \gamma^{(i,j)}\mathbf{I}_s^{(i,j)}, \tag{18}$$

where $\gamma^{(i,j)}$ is the interfacial tension of the (i, j) interface and $\mathbf{I}_s^{(i,j)}$ is the unit surface tensor for the (i, j) interface. In the present case, where the nematic–isotropic interface moves over the substrate, we have:

$$\text{isotropic}-\text{substrate interface}: \mathbf{T}_s^{(I,S)} = \gamma^{(I,S)}\mathbf{I}_s^{(I,S)}; \tag{19a}$$

$$\text{isotropic}-\text{nematic interface}: \mathbf{T}_s^{(I,N)} = \gamma^{(I,N)}\mathbf{I}_s^{(I,N)} - \mathbf{I}_s^{(I,N)}.\left(\frac{\partial\gamma^{(I,N)}}{\partial\mathbf{k}^{(I,N)}}\mathbf{k}^{(I,N)}\right); \tag{19b}$$

$$\text{substrate}-\text{nematic interface}: \mathbf{T}_s^{(S,N)} = \gamma^{(S,N)}\mathbf{I}_s^{(S,N)} - \mathbf{I}_s^{(S,N)}.\left(\frac{\partial\gamma^{(I,N)}}{\partial\mathbf{k}^{(S,N)}}\mathbf{k}^{(S,N)}\right). \tag{19c}$$

The capillary force from the junction sum appearing in equation (15) will expand the nematic volume and reduce the isotropic volume when

$$\sum_{\text{jun}} \mathbf{v}\cdot\mathbf{T}_s\cdot\mathbf{p} = \left(\gamma^{(I,S)} - \gamma^{(S,N)} - \gamma^{(I,N)}\cos\theta\right) - \mathbf{v}^{(I,N)}.\left(\mathbf{I}_s^{(I,N)}.\frac{\partial\gamma^{(I,N)}}{\partial\mathbf{k}^{(I,N)}}\mathbf{k}^{(I,N)}\right)\cdot\mathbf{p} - \mathbf{v}^{(S,N)}.\left(\mathbf{I}_s^{(S,N)}.\frac{\partial\gamma^{(S,N)}}{\partial\mathbf{k}^{(S,N)}}\mathbf{k}^{(S,N)}\right)\cdot\mathbf{p} > 0. \tag{20}$$

In the simplest case, when the energy associated with the contact line is given by an isotropic local free energy or line tension, the line tension contribution in equation (15) is:

$$(\nabla_\ell\bullet\mathbf{T}_\ell)\bullet\mathbf{p} = f_\ell\kappa, \tag{21}$$

where κ is the line curvature. For the straight contact line considered here, $(\nabla_\ell\bullet\mathbf{T}_\ell)\bullet\mathbf{p}=0$ since $\kappa=0$. Finally the dissipation term in equation (15) for a steady line tensor order parameter vanishes: $\mathbf{Q}^\ell : d\mathbf{Q}^\ell/dt = 0$. Hence,

under steady contact line motion, equation (15) simplifies to:

$$\beta_\ell w_\ell = \left(\oint_{\text{jun}} (\mathbf{k} \bullet \mathbf{T}_b) \mathrm{d}\ell + \sum_{\text{jun}} \mathbf{v} \bullet \mathbf{T}_s \right) \bullet \mathbf{p}. \qquad (22)$$

The results summarized in equations (15) and (22) can now be used to classify and qualitatively characterize texturing processes in the various kinetic regimes of the film and droplet phase ordering modes described above.

(i) Film growth: in this regime the kinetics is independent of equation (22). In the presence of substrate heterogeneities different front velocities can be expected across the interface. For a flat planar interface growing from a patch where the orientation is tangential to the substrate ($\mathbf{n}=\mathbf{p}$, $n_z=0$, z-direction normal to the substrate), the interface velocity is:

$$(w_s)_{n=p} = \frac{\Delta f_h}{(\beta_\perp)_{n=p}}, \qquad (23)$$

whereas for film growth from a patch where the director orientation is normal (homeotropic) to the substrate ($\mathbf{n}=\mathbf{k}$) is:

$$(w_s)_{n=k} = \frac{\Delta f_h}{(\beta_\perp)_{n=k}} \qquad (24)$$

As shown elsewhere [37], $(\beta_s)_{\mathbf{n}=\mathbf{p}} > (\beta_s)_{\mathbf{n}=\mathbf{k}}$ and hence we expect that this differential ($|(w_s)_{\mathbf{n}=\mathbf{k}} - (w_s)_{\mathbf{n}=\mathbf{p}}|$) in film growth velocity will result in a cusp formation above the location of the orientation discontinuity. The distance d above the interface can be estimated by the following argument. When the differential speed causes a step whose amplitude is of the order of the nematic correlation length $\xi = \sqrt{L_1/|a(T-T*)|}$ a defect will nucleate on the interface (see figure 3 a). Using equations (23)–(24) we find the distance from the defect to the substrate with planar orientation is:

$$\ell_p = \frac{(\beta_s)_{n=p}}{(\beta_s)_{n=k} - (\beta_s)_{n=p}} \xi. \qquad (25)$$

For the present material properties $\xi \approx 20$ nm and the computations (see figure 8) give $\ell_p \approx 70$ nm, which indicates that $(\beta_s)_{\mathbf{n}=\mathbf{p}}/((\beta_s)_{\mathbf{n}=\mathbf{p}} - (\beta_s)_{\mathbf{n}=\mathbf{k}}) \approx 3.5$. In what follows we refer to this mechanism as interfacial defect shedding.

In the region surrounding an anchoring discontinuity on the substrate, say from planar to homeotropic, surface melting occurs. For simplicity assuming a one constant approximation equation (7) reads:

$$Z - L_1 \nabla^2 \mathbf{Q} = 0, \qquad (26)$$

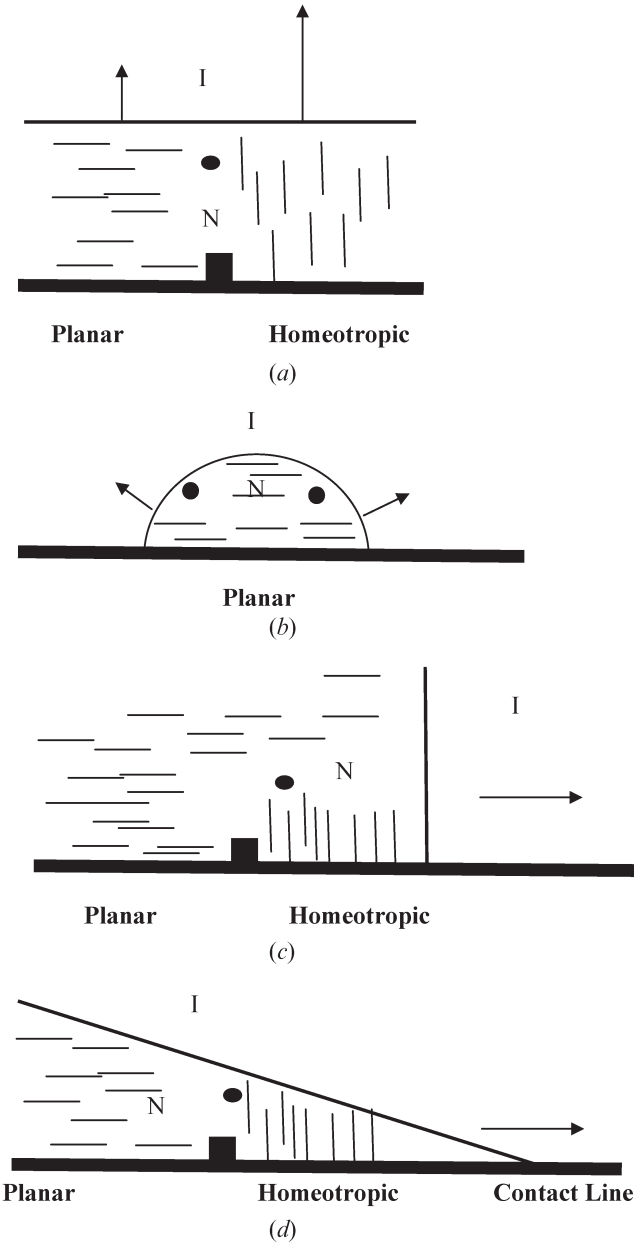

Figure 3. Texturing processes during phase ordering. The dark circle denotes a disclination line of strength ½ and the black square denotes an orientation discontinuity (switch) on the substrate. (a) Film growth over heterogeneous substrates activates interfacial defect shedding (IDS); (b) large curvature droplet growth over a homogeneous substrate activates IDS; (c) drops with large contact angles over orientation switches activates IDS; (d) drops with small contact angles crossing an orientation switch activates IDS.

$$Z = a(T - T*)\mathbf{Q} - B\left[\mathbf{Q}\cdot\mathbf{Q} - \frac{1}{3}\mathbf{Q} : \mathbf{Q}\mathbf{I}\right] + C\mathbf{Q} : \mathbf{Q}\,\mathbf{Q}. \quad (27)$$

Using polar coordinates (ρ, φ) centred at the substrate orientation discontinuity, and assuming a tensor field of the form:

$$\mathbf{Q} = \mathrm{S}(\rho, \varphi)(\mathbf{n}(\varphi)\mathbf{n}(\varphi) - \mathrm{I}/3) + \frac{\mathrm{P}}{3}(\rho, \varphi)(\mathbf{m}(\varphi)\mathbf{m}(\varphi) - \boldsymbol{\delta}_z\boldsymbol{\delta}_z), \quad (28)$$

$$\mathbf{n} = \cos(\varphi/2)\boldsymbol{\delta}_x + \sin(\varphi/2)\boldsymbol{\delta}_y; \quad \mathbf{m} = -\sin(\varphi/2)\boldsymbol{\delta}_x + \cos(\varphi/2)\boldsymbol{\delta}_y;\ \mathbf{l} = \boldsymbol{\delta}_z, \quad (29)$$

it is found that when $P = 1 - S$, the scalar order parameter S obeys [66]:

$$\nabla^2 \mathrm{S} - \frac{(6S-1)}{6\rho^2} - \frac{4}{9L_1}\mathrm{Z} : \mathbf{nn} = 0. \quad (30)$$

Hence, as $\rho \to 0$, $S \to 1/6$. The reduction in S from $S_{eq} = 0.58$ in the vicinity of the discontinuity is referred to as surface melting.

(ii) Droplet growth: this regime involves the coupling between the bulk nematic–isotropic interface dynamics and the substrate–nematic–isotropic contact line dynamics. Observation of equations (11) and (15) indicates that the couplings enter via the bulk stress tensor $\mathbf{T}_b$ and the surface stress tensor $\mathbf{T}_s$ of the nematic–isotropic interface. Quantifying and characterizing the exact nature of the wetting/phase ordering coupling requires the numerical solution to the bulk and interface equations, which requires specific values for all the homogeneous and gradient bulk, interface, and line energies. However, in the absence of such specific information this paper pursues instead a parametric study that provides a general picture of texturing processes of the droplet growth mode under different wetting/phase ordering regimes by assuming a priori a specific relationship between phase ordering and wetting kinematics. We postulate that three wetting-phase ordering regimes are possible:

(i) Passive substrate regime: $w_s = w_\ell$
(ii) Wetting driven regime: $w_s < w_\ell$
(iii) Phase ordering driven regime: $w_s > w_\ell$

In this paper we investigate the first two and leave the third complex case to future work. In terms of thecontact angle, φ, the passive substrate corresponds to contact angles close to π/2, whereas the wetting regime corresponds to small contact angles. We note that the limiting condition of the wetting regime ($w_\perp \ll w_{CL}$, $\varphi \to 0$) is the nucleation of the surface nematic film. The exact homogeneous and gradient bulk, interfacial, and line energies that lead to the selected regimes are left for future work. Here we are interested in identifying the texturing and defect nucleation processes that arise for a given wetting-phase ordering regime. It is noted that surface melting will always occur, regardless of the contact line speed.

For the passive substrate regime ($w_\perp = w_{CL}$, $\varphi \approx \pi/2$) we find that if the drop nucleates in a homogeneous region (say, planar) and if the contact angle is large enough then interfacial defect shedding will occur (see figure 3 b). The reason is that the nematic–isotropic interface is no longer homogeneous with respect to director orientation and hence differential speed creates an unstable cusp that eventually sheds a defect. For conditions close to the passive substrate regime the contact angle is large and close to π/2. When crossing an orientation discontinuity on the substrate, say from planar to homeotropic, again leads to interfacial defect shedding since the interface is heterogeneous: close to the contact line it is homeotropic and far from the contact line it will be planar (see figure 3 c).

For the wetting driven regime ($w_\perp < w_{CL}\sin\varphi$), when the contact angle is relatively small defect shedding will not occur within a homogeneous substrate region because the nematic-isotropic interface is not sufficiently heterogeneous to cause a significant speed differential effect. On the other hand, since the contact angle is relatively small, when the contact line traverses a substrate discontinuity the defect shedding mechanism is activated just as in the case of film growth (see figure 3 d).

Lastly we comment on the overall orientation of the disclination line that arises through interfacial defect shedding for both film and drop regimes. The disclination lines that arise in this work are all of strength ½, and the planar director field around the disclination is approximately given by:

$$\psi = \frac{1}{2}\varphi + c \quad (31)$$

where the constant c defines the overall orientation of the defect and ψ is the director orientation angle at the radial coordinate ρ of the polar coordinate system (φ, ρ) attached to the defect core [67]. It turns out that interfacial defect shedding will result in a specific overall orientation of the defect depending on whether the process is a film or droplet growth process. For film processes with planar-homeotropic anchoring, the overall orientation of the defect is described by $c = \pi/2$ (see figure 8, 10 μs). For large curvature droplets growing over a homogeneous homeotropic substrate the overall orientation of the defect is described by $c = 3\pi/4$ (figure 4, 10 μs); the planar case was not investigated.

For drops with small contact angles the overall orientation of the defect is as in the film growth case (figure 7, 10 μs). Finally for drops spreading with large contact angles, the overall orientation of the defect is described by $c=3\pi/4$ (figure 5, 10 μs).

In partial summary, simple arguments based on contact line and interfacial front kinetics as well as discontinuities on the substrate leads to the expectation of the following texturing processes:

(1) Surface melting: these are subsurface defects that arise whenever there are substrate discontinuities;
(2) Interfacial defect shedding: this mechanism arises under droplet growth and under film growth, as follows. Film growth over a heterogeneous substrate will shed a defect over the discontinuity (figure 3 a). Droplet growth for sufficiently small contact angles (wetting regime) over a heterogeneous substrate will also shed a defect due to the same reason as in the film case (figure 3 d). This mechanism is also activated for droplet growth over passive and homogeneous substrates because the nematic-isotropic interface is sufficiently heterogeneous (figure 3 b). Finally, a sufficiently large contact angle moving across discontinuities also leads to defect shedding (figure 3 c). Below we show that direct numerical simulation confirms these predictions.

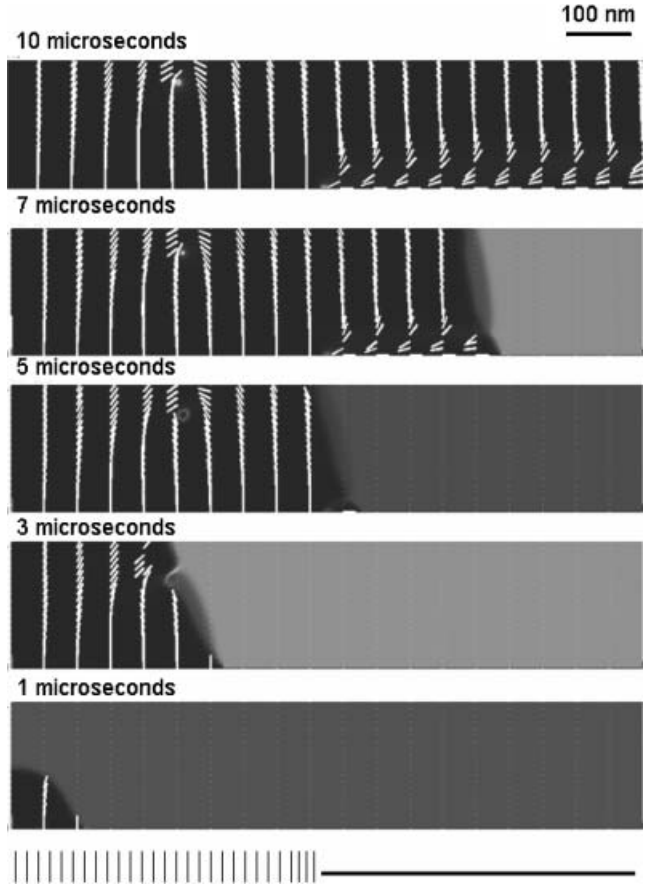

Figure 4. Nematic textures for 5CB occurring 1, 3, 5, 7 and 10 μs after an isotropic-to-nematic quench (25°C) for droplet nucleation on a strongly anchored decorated surface. Growth of the nematic phase begins from a single nucleation located within 10 nm on the left of the surface (droplet regime). The surface has one switch in anchoring such that to the left (right) of the switch, the liquid crystal surface anchoring is homeotropic (planar). The speed at which the nematic phase moves across the surface was set to match that in the bulk ($0.11\,m\,s^{-1}$). Short white lines=director orientation. White dots or loops identify defects. Scale bar=100 nm. The darker (lighter) background indicates a nematic (isotropic) phase. At 3 μs, interfacial defect shedding begins as the high curvature nematic droplet grows over a homogeneous patch of the substrate. By 5 μs, this defect mechanism has deposited a +1/2 defect into the bulk nematic phase. In addition, when the phase transition occurs at the surface anchoring switch, a high energy region (white) indicates that surface melting has occurred (5 μs).

3. Computational modelling

To better understand the formation of nematic textures near a decorated surface, we simulate the time evolution of the tensor order parameter **Q** in a semi-infinite two-dimensional computational domain, where the bottom boundary is the decorated surface. Since the second rank tensor order parameter (symmetric and traceless) has five independent components, this requires that five coupled time-dependent nonlinear partial differential equations be solved simultaneously. We consider a quench of 5CB to a temperature of $T=25^{\circ}C$. For the droplet mode we focus on one small region along the surface where 10 nm at the left-most part of the bottom boundary has nucleated to the nematic phase. From this small surface nucleation, the nematic phase grows into the unstable isotropic bulk and along the surface, resulting in the dynamic formation of a liquid crystal texture near the solid surface. The rate at which the nematic phase (i) grows into the bulk and (ii) along the surface is not necessarily equal, as explained above.

3.1. *Initial conditions (nucleation) and the isotropic phase*

A surface droplet nucleation is implemented in our simulations by initially setting the tensor order parameter to its nematic value in a small 10 nm region that is located at the left-most part of the bottom boundary, with the tensor order parameter in the rest of the domain set to a very small isotropic value. In the nucleated region for $T=25^{\circ}C$, the nematic phase of the liquid crystal 5CB is uniaxial with $S=0.5788$ and $P=0$ [52]. We assume that a nematic region can grow undisturbed for at least 2 μm. For surface films, the

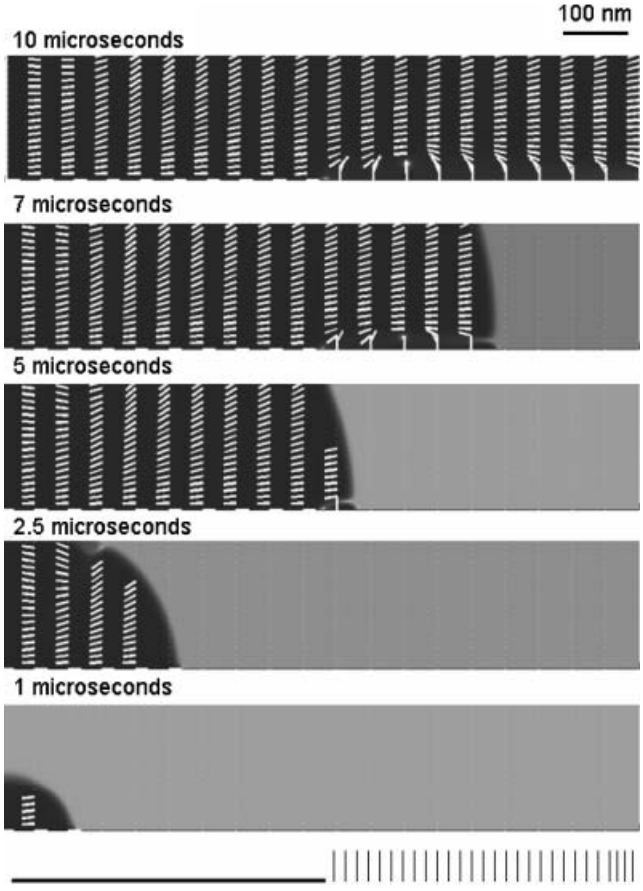

Figure 5. Nematic textures for 5CB occurring 1, 2.5, 5, 7 and 10 μs after an isotropic-to-nematic quench (25°C) for droplet nucleation on a strongly anchored decorated surface. Growth of the nematic phase begins from a single nucleation located within 10 nm on the left of the surface (droplet regime). The surface has one switch in anchoring such that to the left (right) of the switch, the liquid crystal surface anchoring is planar (homeotropic). The speed at which the nematic phase moves across the surface was set to match that in the bulk ($0.11\,\mathrm{m\,s^{-1}}$), so that an 80° contact angle occurs between the nematic–substrate and nematic–isotropic interfaces at the anchoring switch. Short white lines=director orientation. White dots or loops identify defects. Scale bar=100 nm. The darker (lighter) background indicates a nematic (isotropic) phase. The large contact angle of 80° at the anchoring switch triggers interfacial defect shedding (5 μs). By 7 μs, this defect mechanism has created a bulk +1/2 defect located 25 nm above the solid surface and 130 nm beyond the anchoring switch. The overall orientation of this +1/2 defect is given by $c=3\pi/4$. The high energy region (white) located exactly at the anchoring switch on the substrate indicates that surface melting has also occurred.

initial state is a thin nematic film where the order parameter is $S=0.5788$ across the substrate and the orientation is fixed but heterogeneous.

It is important to maintain appropriate tensor order parameter values for the isotropic phase that is not in contact with the growing nematic. Otherwise, as time progresses, the TDGL model predicts that the entire domain converts to the nematic phase simultaneously and instantaneously, rather than through a nucleation and growth process. We expect that a lower temperature quench results in a higher density of nucleations and that the growth of these nucleations occurs at a very fast time scale. Considering the phase transition at too large a length and time scale ignores defects and deformations on the submicron level which may be important to the formation of the actual textures experimentally observed in liquid crystal sensors with nano-decorated surfaces.

To achieve nucleation and growth in the simulations, the movement of the nematic–isotropic interface is monitored and the isotropic phase is reset to small tensor order parameter values ahead of the isotropic edge of the moving front.

3.2. *Boundary conditions*

After the nematic phase has initially nucleated on a small region of the surface, we consider this to trigger further nematic growth along the surface. Because this growth along the surface is dynamic, at the bottom boundary which represents the decorated surface, a time-dependent Dirichlet boundary condition is used. Along the decorated surface not yet touched by the nematic phase, the tensor order parameter $\mathbf{Q}$ is set to a very small isotropic value. Imposing a nematic growth rate along the decorated surface, the Dirichlet bottom boundary conditions are recalculated as the numerical solver steps forward in time. When a region along the decorated surface is meant to become nematic, its isotropic tensors along the bottom boundary become uniaxial nematic tensors ($S=0.5788$, $P=0$). Once nematic, these bottom boundary tensors are fixed, i.e. their orientation and magnitude do not change with time, to represent a strong anchoring surface.

The semi-infinite top, left, and right boundaries are passive and therefore modelled with Neumann boundary conditions:

$$\text{Top boundary}: \quad \frac{\partial \mathbf{Q}}{\partial y} = 0 \tag{32}$$

$$\text{Left and right boundaries}: \quad \frac{\partial \mathbf{Q}}{\partial x} = 0 \tag{33}$$

3.3. *Numerical methods*

The finite element method software package FEMLAB 3.1a was used to solve the five coupled time-dependent nonlinear partial differential equations, by applying the direct UMFPACK solver method and the

time-dependent backward Euler method. All time steps taken were smaller than 100 ns. To physically interpret the calculated tensor order parameter, its eigenvectors and eigenvalues were calculated using the **eig** function in MATLAB. To calculate the free energy of the system, the free energy density of the system described by the Landau–de Gennes equation (taking the isotropic phase as the reference point) was integrated element-wise using a fourth order numerical quadrature.

4. Results and discussion

4.1. *Droplet growth regime*

4.1.1. Two texturing modes: surface melting and interfacial defect shedding. Figure 4 shows the dynamic early stage development of defects and deformations in the 5CB liquid crystal phase above a strongly anchored decorated solid surface after an isotropic-to-nematic quench at 25°C. Growth of the nematic phase begins from a single surface nucleation located within 10 nm on the left of the surface. The surface has one switch in anchoring such that to the left (right) of the switch, the liquid crystal surface anchoring is homeotropic (planar). The speed at which the nematic phase moves across the surface was set to match that in the bulk, which was $0.11\,\mathrm{m\,s^{-1}}$ due to the chosen 5CB bulk material parameters (a, B, C, L_1, L_2, L_3 and β given in section 2.2). The short white lines in figure 4 indicate the orientation of the nematic director and the white dots or loops identify defects. The darker (lighter) background indicates a nematic (isotropic) phase. As the nematic phase grows from the surface nucleation, two different high energy defect regions appear: (i) at the surface, where the anchoring changes from homeotropic to planar, and (ii) in the bulk before the nematic phase contacts the anchoring switch, i.e. 140 nm above the solid surface and 250 nm to the right of the nematic surface nucleation. To avoid the high free energy of an extreme nematic surface orientation gradient, surface melting occurs exactly at the homeotropic-planar anchoring switch creating a defect. In contrast, the bulk defect forms due to an anchoring conflicting at the highly curved advancing isotropic-nematic interface. As the front advances, the interfacial anchoring conflict is resolved by leaving behind a +1/2 bulk defect. This situation is known as interfacial defect shedding, a new recently predicted defect forming mechanism observed in simulations for growing nematic nanodroplets [36–38, 68]. In the nanodroplet simulations, an advancing high curvature isotropic–nematic interface leads to opposing nematic anchoring along the moving isotropic–nematic interface, defect cores form within the interface, and then +1/2 defects are shed from the interface into the bulk nematic phase.

4.1.2. Contact angle. Imposing a new speed for the contact line along the solid surface yields different contact angles between the isotropic–nematic interface and the solid surface. Table 1 shows three different contact line speeds and the resulting contact angle when the nematic phase arrives at a planar-to-homeotropic anchoring switch located 500 nm from the initial surface nucleation. For example, when the nematic front moves with the same velocity (i) in the bulk and (ii) along the surface, it makes a contact angle of 80° with the solid surface at the anchoring switch. When the nematic front travels 1.5 times faster along the surface than in the bulk, a much smaller 35° contact angle occurs at the anchoring switch.

Figures 5–7 show the computational results for a strongly anchored flat solid surface with one planar-to-homeotropic anchoring switch located 500 nm from the initial nematic surface nucleation, where the contact angle at the surface switch is 80°, 35° and 20°, respectively. In all of these figures there is, not surprisingly, a defect occurring at the surface at the anchoring switch due to surface melting. In contrast, for bulk defects, the contact angle determines if interfacial defect shedding occurs and the overall orientation of the +1/2 defect. In figure 5, the larger contact angle of 80° at the anchoring switch yields a +1/2 bulk defect with $c=3\pi/4$ that is 25 nm above the solid surface and 130 nm beyond the anchoring switch.

However, for a contact angle of 35° (figure 6), whereas the surface switch still causes an orientation transition along the isotropic-nematic interface, the resulting gradient in the interfacial tensor order parameter is not enough to nucleate a bulk defect.

A smaller contact angle of 20° (figure 7), does create a +1/2 bulk defect through interfacial defect shedding. In contrast to the +1/2 bulk defect created from an 80° contact angle (figure 5), the +1/2 bulk defect due to a contact angle of 20° (figure 7) has an overall orientation described by $c=\pi/2$. In addition, the bulk defect created at the smaller contact angle occurs sooner after the surface anchoring switch, but farther above the solid surface.

Table 1. Contact angle and contact line speeds.

	Bulk speed (nematic–isotropic interface) /m s^{-1}	Contact line speed /m s^{-1}	Contact angle (500 nm from surface nucleation)/°
Figure 5	0.11	0.11	80
Figure 6	0.11	1.5×0.11	35
Figure 7	0.11	2×0.11	20
Figure 8	0.11	$\gg0.11$	0

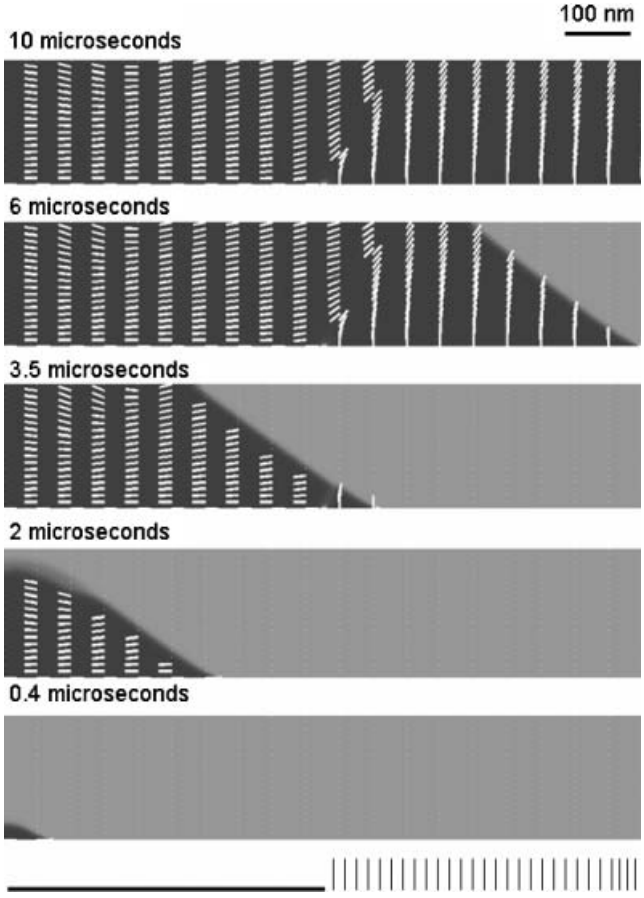

Figure 6. Nematic textures for 5CB occurring 0.4, 2, 3.5, 6 and 10 μs after an isotropic-to-nematic quench (25°C) for droplet nucleation on a strongly anchored decorated surface. Growth of the nematic phase begins from a single nucleation located within 10 nm on the left of the surface (droplet regime). The surface has one switch in anchoring such that to the left (right) of the switch, the liquid crystal surface anchoring is planar (homeotropic). The contact line speed was set to $1.5 \times 0.11\,\mathrm{m\,s^{-1}}$, so that a 35° contact angle occurs between the nematic–substrate and nematic–isotropic interfaces at the anchoring switch. Short white lines=director orientation. White dots or loops identify defects. Scale bar=100 nm. The darker (lighter) background indicates a nematic (isotropic) phase. The contact angle of 35° at the anchoring switch does not cause extreme interfacial ordering gradients along the isotropic–nematic interface so interfacial defect shedding is not triggered. Instead, the nematic phase texture shows a smooth deformation away from the planar orientation when moving above the homeotropic anchored surface. The high energy region (white) located exactly at the anchoring switch on the substrate (10 μs) indicates that surface melting has occurred.

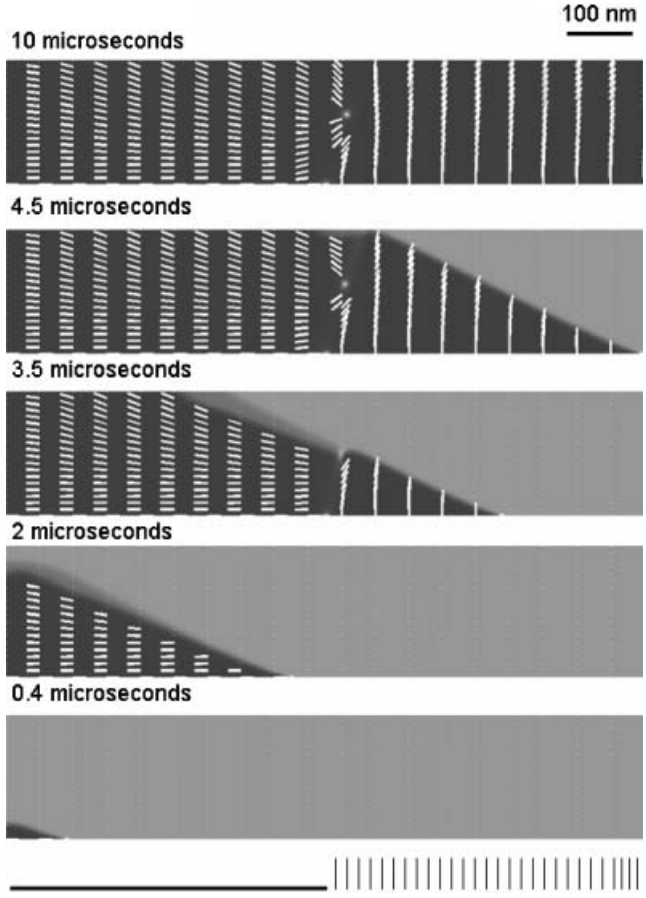

Figure 7. Nematic textures for 5CB occurring 0.4, 2, 3.5, 4.5 and 10 μs after an isotropic-to-nematic quench (25°C) for droplet nucleation on a strongly anchored decorated surface. Growth of the nematic phase begins from a single nucleation located within 10 nm on the left of the surface (droplet regime). The surface has one switch in anchoring such that to the left (right) of the switch, the liquid crystal surface anchoring is planar (homeotropic). The speed at which the nematic phase moves across the surface was set to $2 \times 0.11\,\mathrm{m\,s^{-1}}$, so that a 20° contact angle occurs between the nematic–substrate and nematic–isotropic interfaces at the anchoring switch. Short white lines=director orientation. White dots or loops identify defects. Scale bar=100 nm. The darker (lighter) background indicates a nematic (isotropic) phase. The small contact angle of 20° at the anchoring switch triggers interfacial defect shedding (3.5 μs). By 4.5 μs, this defect mechanism has created a bulk +1/2 defect with $c=\pi/2$ located 100 nm above the solid surface just beyond the anchoring switch. The high energy region (white) located exactly at the anchoring switch on the substrate (10 μs) indicates that surface melting has also occurred.

4.2. *Film growth regime*

In figure 8, the nematic phase nucleates along the entire solid substrate and then grows normal to the surface into the bulk. This type of behaviour has been observed for 5CB on rubbed PVA surfaces where the nematic phase nucleates a uniform layer adjacent to the substrate rather than at the scratches or substrate defects which are usually thought to act as nucleation sites [34]. This nematic film nucleation is believed to be crucially related to the existence of a highly ordered layer in the isotropic phase next to the ordering solid substrate, i.e. a

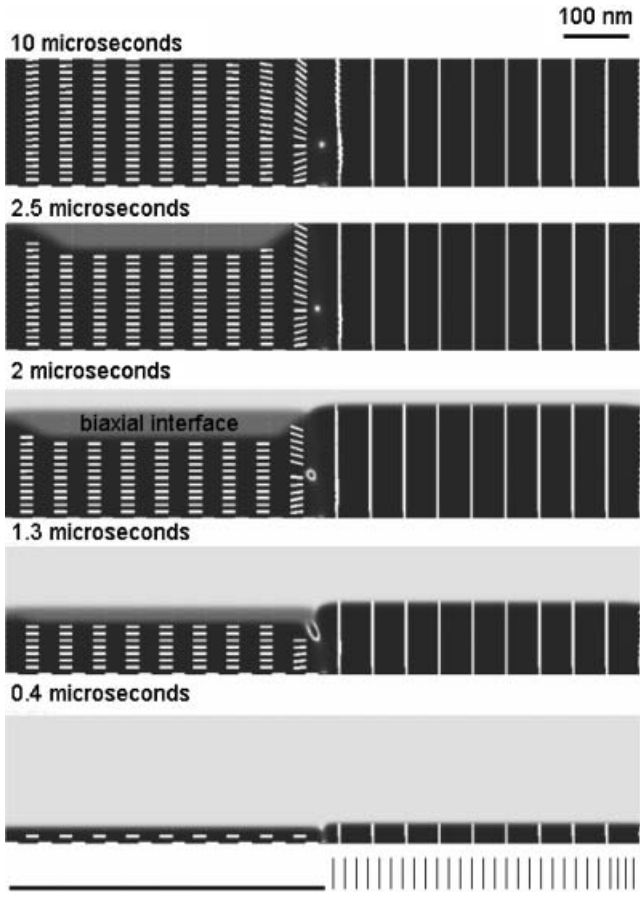

Figure 8. Nematic textures for 5CB occurring 0.4, 1.3, 2, 2.5 and 10 μs after a nematic surface film arises through a surface phase transition that covers the entire substrate (wetting regime, $\gamma_{is}>\gamma_{ns}+\gamma_{in}$) after an isotropic-to-nematic quench (25°C) on a strongly anchored decorated surface. The isotropic–nematic interface then grows up from the decorated substrate. The surface has one switch in anchoring such that to the left (right) of the switch, the liquid crystal surface anchoring is planar (homeotropic). Short white lines=director orientation. White dots or loops identify defects. Scale bar=100 nm. The darker (lighter) background indicates a nematic (isotropic) phase. At 0.4 μs, the nematic phase is found within 25 nm of the surface and the nematic texture is controlled by the solid surface anchoring, i.e. the nematic is weakly anchored at the isotropic–nematic interface. By 1.3 μs, a triple line occurs at the nematic front where the nematic, biaxial and uniaxial interface phases meet at a high energy region with opposing nematic directors. As the front advances, the high free energy region is trapped into the nematic phase, through the interfacial defect shedding mechanism, in the form of a disclination ring (2 μs), which shrinks to a +1/2 bulk defect with $c=\pi/2$ located 70 nm directly above the anchoring switch (2.5 μs). Given that this defect does not move or disappear (10 μs), the computational results suggest that bulk defects created by interfacial defect shedding are stable with respect to the decorated surface during the early stage dynamics of nematic phase formation. The high energy region (white) located exactly at the anchoring switch on the substrate indicates that surface melting also occurs very soon after the nematic surface film forms (0.4 μs).

paranematic phase, and is analogous to the condensation of a vapour on a wet substrate [34]. The same decorated surface of figures 5–7 is also used in figure 8. As the isotropic–nematic interface grows up from the flat decorated substrate, a +1/2 bulk defect forms at 70 nm directly above the solid surface anchoring switch.

Figure 8 illustrates clearly some of the important characteristics for interfacial defect shedding from a relatively flat interface. When the nematic phase nucleates as a uniform layer along the flat solid decorated surface, it begins to grow upwards into the unstable isotropic phase. After a short time of 0.4 μs, the nematic phase is found only within 25 nm of the surface and the nematic texture is controlled by the solid surface anchoring i.e. the nematic is weakly anchored at the isotropic-nematic interface. Using a material such as 5CB that is even only slightly elastically anisotropic (bend energy penalty>splay energy penalty>twist energy penalty), our simulations indicate that as the nematic continues to grow, the structure of the nematic–isotropic interface is not identical at all points. In our computational results, the orientation at and within the moving interface is not imposed, but rather is self-selected as the system grows the nematic phase into the isotropic phase to minimize its free energy. As nematic growth continues, the distinct regions of homeotropic and planar orientation along the isotropic-nematic interface correspond to different interface structures. Figures 9–10 plot the eigenvalues for the planar and homeotropically anchored interface structures, respectively. Such differences in isotropic-nematic interface structures have also been observed by others using a similar Landau–de Gennes model [40]. An analysis of the eigenvalues in figure 10 indicates that when the nematic orientation is normal to the interface, a uniaxial nematic-to-isotropic structure with no rotation of the eigenframe occurs across the small (~50 nm) isotropic–nematic interface region. However, when the nematic director is planar to the interface (figure 9), there is a more complicated ordering structure that occurs across a larger (~90 nm) interface: (i) uniaxial nematic to (ii) biaxial state to (iii) planar degenerate biaxial state with an orthogonal director to (iv) isotropic. The orthogonal director transition between the first and second biaxial states is due to an eigenvalue exchange. The evolution of both homeotropic and planar anchoring at the nematic interface occurs because the interfacial anchoring is weak enough that the interfacial tension alone does not dictate the nematic anchoring. As the nematic–isotropic interface moves further from the solid surface, the result of this energetically driven optimization along the nematic-isotropic interface results in a triple line at the nematic front where the nematic, biaxial and

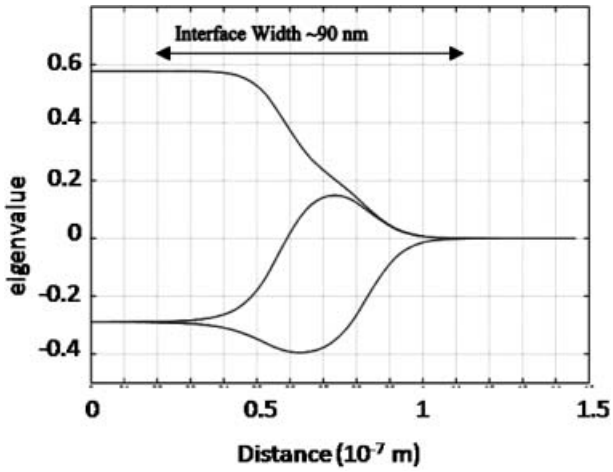

Figure 9. Eigenvalues across a planar anchored biaxial nematic–isotropic interface. Since the nematic director is planar to the interface, there is a complicated ordering structure that occurs across the large (~90 nm) interface: (i) uniaxial nematic to (ii) biaxial state to (iii) planar degenerate biaxial state with an orthogonal director to (iv) isotropic. The orthogonal director transition between the first and second biaxial states is due to an eigenvalue exchange.

uniaxial interface phases meet at a high energy region with opposing nematic directors (figure 8, 1.3 μs). As the front advances, the high free energy region is trapped into the nematic phase in the form of a disclination ring (figure 8, 2 μs), which shrinks to a +1/2 bulk defect (figure 8, 2.5 μs). Given that this defect does not move or disappear even after 10 μs, the computational results suggest that bulk defects created by interfacial defect shedding are stable with respect to the decorated surface during the early stage dynamics of nematic phase formation.

4.3. *Multiple anchoring switches*

Next, a decorated surface with multiple anchoring switches is considered. This situation is of interest as previous numerical simulations for 5CB texture coarsening have indicated that when nanoparticles adsorb to and disrupt aligning solid surfaces, their adsorption pattern, in addition to the total surface coverage of the nanoparticles, has an important influence on the bulk nematic texture [69]. In figure 11, the decorated surface contains four surface anchoring switches between five

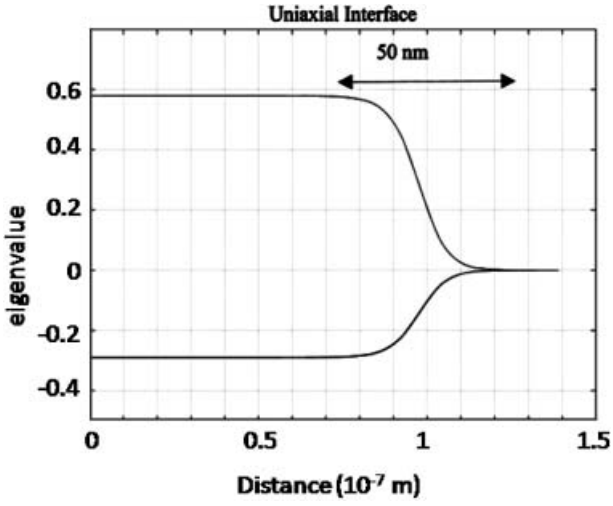

Figure 10. Eigenvalues across a homeotropic anchored uniaxial nematic–isotropic interface. Since the nematic orientation is normal to the interface, a simple uniaxial nematic-to-isotropic structure with no rotation of the eigenframe and no biaxiality occurs across the small (~50 nm) isotropic–nematic interface region.

patches of alternating planar and homeotropic anchoring. After the nematic front has passed the first planar-to-homeotropic surface anchoring switch (figure 11, 2.5 μs), a streak of high energy occurs in the nematic material 25 nm above the homeotropically anchored surface. However, because of the high curvature of the isotropic-nematic interface, a bulk defect does not form above the homeotropic surface. This combination of an anchoring switch and a highly curved isotropic–nematic interface prevents interfacial defect shedding. Then the isotropic–nematic interface shape becomes less curved as it moves towards the second planar-to-homeotropic anchoring switch (figure 11, 8 μs) because the nematic region is expanding. Here, the contact between a flatter isotropic-nematic interface and the anchoring switch does cause interfacial defect shedding and a +1/2 bulk defect situated 25 nm above the second patch of solid surface homeotropic anchoring is shed from the isotropic-nematic interface into the bulk nematic phase. Figures 4, 5 and 11 illustrate that knowledge of the curvature of the isotropic–nematic interface and the surface decoration is important when determining how and why bulk defects will form during the early stages in a nematic phase growing above a flat decorated surface.

4.4. *Free energy*

Figure 12 is a typical result from the above simulations, where the total free energy of the system decreases as the propagating front reduces the isotropic volume fraction. The nematic–isotropic interface in our simulations moves with a self-selected bulk velocity of $0.11\,\mathrm{m\,s^{-1}}$ at the isotropic edge of the interface due to the material properties of 5CB. In addition, figure 12 shows that the average free energy density of the non-isotropic region, i.e. the nematic and interface regions taken together also decreases during the growth process. This indicates that the reduction of the isotropic volume fraction is not the only source of free energy optimization, but that dynamic changes in structure within the combined nematic and interface regions also contribute to reduce the free energy of the system. Since we do not observe a complete alignment of the bulk nematic phase nor do we observe uniform anchoring along the isotropic–nematic interface, the model must be dynamically minimizing the average free energy density of the two regions taken together. This helps to explain why the model predicts dynamic nematic textures that lead to interfacial defect shedding and +1/2 bulk defects above a decorated surface, in addition to the expected surface melting at anchoring switches.

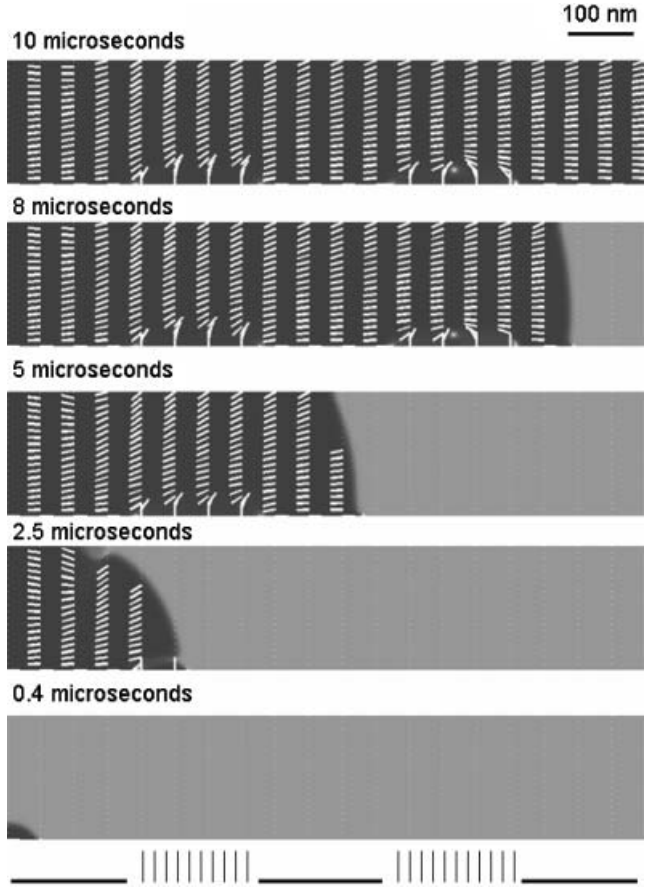

Figure 11. Nematic textures for 5CB occurring 0.4, 2.5, 5, 8 and 10 μs after an isotropic-to-nematic quench (25°C) for droplet nucleation on a strongly anchored decorated surface. Growth of the nematic phase begins from a single nucleation located within 10 nm on the left of the surface (droplet regime). The decorated surface contains four surface anchoring switches between five patches of alternating planar and homeotropic strong anchoring. The speed at which the nematic phase moves across the surface was set to match that in the bulk ($0.11\,\mathrm{m\,s^{-1}}$). Short white lines=director orientation. White dots or loops identify defects. Scale bar=100 nm. The darker (lighter) background indicates a nematic (isotropic) phase. The high energy regions (white) located exactly at each anchoring switch on the substrate indicate surface melting has occurred (10 μs). After the nematic front has passed the first planar-to-homeotropic surface anchoring switch (2.5 μs), a streak of high energy occurs in the nematic material 25 nm above the homeotropically anchored surface. But the combination of an anchoring switch and a highly curved isotropic-nematic interface prevents interfacial defect shedding. As the isotropic-nematic interface propagates forward, its shape becomes less highly curved because the nematic region is expanding (5 μs). After encountering the second planar-to-homeotropic surface anchoring switch (8 μs), contact between a flatter isotropic-nematic interface and the anchoring switch does cause interfacial defect shedding and a +1/2 bulk defect with $c=3\pi/4$ situated 25 nm above the second patch of solid surface homeotropic anchoring occurs. This figure illustrates that knowledge of the curvature of the isotropic–nematic interface and the surface decoration is important when determining how and why bulk defects will form during the early stages in a nematic phase growing above a flat decorated surface.

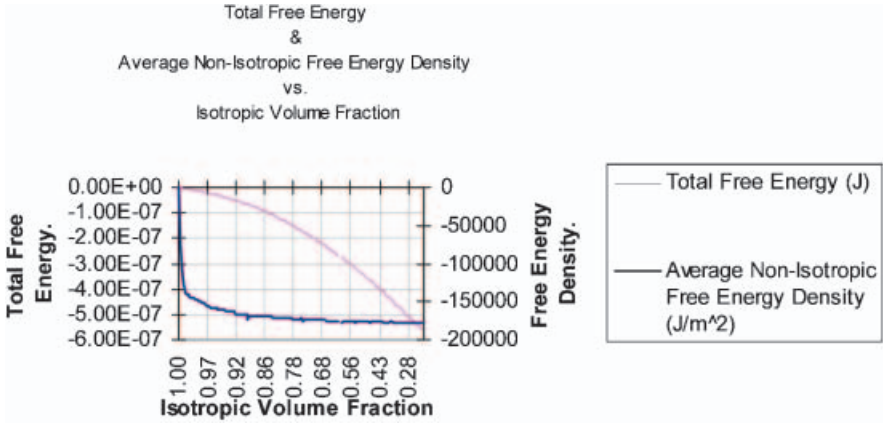

Figure 12. Total free energy (light solid line, in J) and average non-isotropic free energy density (heavy solid line, in $J\,m^{-2}$) during front propagation for an isotropic-to-nematic phase transition above a decorated surface. Initially, the entire volume of the system is in the isotropic phase and therefore the isotropic volume fraction=1. As the nematic front propagates, the isotropic volume fraction of the system decreases. Non-isotropic free energy density is defined as the free energy density of the bulk nematic phase+nematic–isotropic interface, but not the bulk isotropic phase. As expected, the total free energy of the system decreases as the propagating front reduces the isotropic volume fraction. In addition, the average free energy density of the non-isotropic region i.e. the nematic and interface regions taken together, also decreases during the growth process. This indicates that the reduction of the isotropic volume fraction is not the only source of free energy optimization, but that dynamic changes in structure within the combined nematic and interface regions also contribute to reduce the free energy of the system. This helps to explain why the model predicts dynamic nematic textures that lead to interfacial defect shedding and +1/2 bulk defects above a decorated surface, in addition to the expected surface melting at anchoring switches.

5. Conclusions

In conclusion, the TDGL model and a Landau–de Gennes constitutive equation are based on the principle that the driving force for the isotropic-to-nematic phase transition is a free energy minimization, where at 25°C, liquid crystal 5CB prefers to be in the nematic, rather than the isotropic, phase. As more system volume is converted from isotropic to nematic material by the propagating isotropic-nematic front, the free energy of the system decreases. In addition, the model predicts an additional dynamic reduction of the free energy by decreasing the average free energy density within the bulk nematic and the isotropic-nematic interfacial region, all while under the constraint of a strong anchored decorated solid surface. Because of this coupling, the ordering structure within the nematic-isotropic interface is modified and bulk nematic distortions develop. According to our computational results, this can lead to interfacial defect shedding where a defect core forms in the moving isotropic–nematic interface and then sheds into the bulk nematic phase to create a +1/2 defect. Interfacial defect shedding and surface melting at anchoring switches are both responsible for the formation of defects near a decorated strong anchoring solid surface in early stage nematic textures. Interfacial defect shedding occurs at highly curved nematic–isotropic interfaces next to uniform solid surfaces or from a flatter nematic–isotropic interface whose contact line crosses a solid surface anchoring switch with the appropriate contact angle. Figure 3 gives a summary of the interface defect shedding texturing processes beyond the expected surface melting. Drops with large curvature growing over homogeneous patches, film growth over a switch, and large contact angle flat fronts over a switch all create near-surface disclinations of strength ½. The transient development of different isotropic-nematic interface transitions, proximity to a flat strongly anchored decorated surface, and the curvature of the propagating each play an important role in early stage nematic texturing.

These new results contribute to the on going development of new liquid crystal-based biosensors, where the sensor signal is based on texturing processes that are generated at heterogeneous substrates. More precise models will have to solve the contact line equations coupled to the bulk equation in 3D geometries.

Acknowledgements

This work was supported by a grant from Natural Science and Engineering Research Council of Canada. BW is grateful for financial support from a Eugenie Ulmer Lamothe scholarship at McGill University.

References

[1] P.G. de Gennes, J. Prost. *The Physics of Liquid Crystals*, second edn, Clarendon Press, Oxford (1993).

[2] P.K. Son, J.H. Park, J.C. Kim, T-H. Yoon. *Thin Solid Films*, **515**, 3102 (2007).
[3] P. Pagliusi, C.Y. Chen, Y.R. Shen. *J. chem. Phys.*, **125**, 201104 (2006).
[4] J-Y. Hwang, S-H. Kim, S-H. Choi, H-K. Kang, J-H. Choi, M-H. Ham, J-M. Myoung, D-S. Seo. *Ferroelectrics*, **344**, 191 (2006).
[5] J-S. Park, C-H. Jang, M.L. Tingey, A.M. Lowe, N.L. Abbott. *J. Colloid Interface Sci.*, **304**, 459 (2006).
[6] H-R. Kim, J-H. Kim, T-S. Kim, S-W. Oh, E-Y. Choi. *Appl. Phys. Lett.*, **87**, 143901 (2005).
[7] B.H. Clare, O. Guzman, J. de Pablo, N.L. Abbott. *Langmuir*, **22**, 7776 (2006).
[8] M.G. Tomilin, S.A. Povzun, E.V. Gribanova, T.A. Efimova. *Mol. Cryst. liq. Cryst.*, **367**, 133 (2001).
[9] J.J. Skaife, N.L. Abbott. *Langmuir*, **17**, 5595 (2001).
[10] M.G. Tomilin, A.A. Kilanov, S.A. Povzun. *Mol. Cryst. liq. Cryst.*, **351**, 1 (2000).
[11] J.J. Skaife, N.L. Abbott. *Langmuir*, **16**, 3529 (2000).
[12] V.K. Gupta, T.B. Dubrovsky, N.L. Abbott. *Science*, **279**, 2077 (1998).
[13] J.J. Skaife, J.M. Brake, N.L. Abbott. *Langmuir*, **17**, 5448 (2001).
[14] S.R. Kim, N.L. Abbott. *Adv. Mater.*, **13**, 1445 (2001).
[15] J.A. Van Nelson, S.R. Kim, N.L. Abbott. *Langmuir*, **18**, 5031 (2002).
[16] B.H. Clare, N.L. Abbott. *Langmuir*, **21**, 6451 (2005).
[17] S.R. Kim, R.R. Shah, N.L. Abbott. *Analyt. Chem.*, **72**, 4646 (2000).
[18] Y. Choi, Y. Lee, H. Kwon, S.D. Lee. *Mater. Sci. Engng*, **C24**, 237 (2004).
[19] S.V. Shiyanovskii, O.D. Lavrentovich, T. Schneider, T. Ishikawa, I.I. Smalyukh, C.J. Woolverton, G.D. Niehaus, K.J. Doane. *Mol. Cryst. liq. Cryst.*, **434**, 587 (2005).
[20] S.V. Shiyanovskii, T. Schneider, I.I. Smalyukh, T. Ishikawa, G.D. Niehaus, K.J. Doane, C.J. Woolverton, O.D. Lavrentovich. *Phys. Rev. E*, **71**, 020702 (2005).
[21] S. Grollau, O. Gruzman, N.L. Abbott, J.J. de Pablo. *J. chem. Phys.*, **122**, 024703 (2005).
[22] I. Chuang, R. Durrer, N. Turok, B. Yurke. *Science*, **251**, 1336 (1991).
[23] F. Elias, S.M. Clarke, R. Peck, E.M. Terentjev. *Europhys. Lett.*, **47**, 442 (1999).
[24] G. De Luca, A.D. Rey. *J. chem. Phys.*, **124**, 144904 (2006).
[25] D.K. Ding, E.L. Thomas. *Mol. Cryst. liq. Cryst.*, **241**, 103 (1994).
[26] T. Tsuji, A.D. Rey. *Macromol. Theory Simul.*, **7**, 623 (1998).
[27] V. Popa-Nita. *Eur. Phys. J. B*, **12**, 83 (1999).
[28] M.I. Boamfa, M.W. Kim, J.C. Maan, T. Rasing. *Nature*, **421**, 149 (2003).
[29] Y. Iwashita, H. Tanaka. *Phys. Rev. Lett.*, **95**, 047801 (2005).
[30] J. Ignes-Mullol, J. Baudry, L. Lejcek, P. Oswald. *Phys. Rev. E*, **59**, 568 (1999).
[31] P. Oswald, J. Bechhoefer, A. Libchaber. *Phys. Rev. Lett.*, **58**, 2318 (1987).
[32] J. Bechhoefer, S.A. Langer. *Phys. Rev. E*, **51**, 2356 (1995).
[33] M.J. Bowick, L. Chander, E.A. Schiff, A.M. Srivastava. *Science*, **263**, 943 (1994).
[34] H. Yokoyama, S. Kobayashi, H. Kamei. *Appl. Phys. Lett.*, **41**, 438 (1982).
[35] A. Koehler, H.H. Dunger, E. Dietel. *Z. phys. Chem., Leipzig*, **257**, 1049 (1976).
[36] B. Wincure, A.D. Rey. *J. chem. Phys.*, **124**, 244902 (2006).
[37] B. Wincure, A.D. Rey. *Continuum Mech. Thermodyn.*, **19**, 37 (2007).
[38] B. Wincure, A.D. Rey. *Nano Lett.*, **7**, 1474 (2007).
[39] Y. Lansac, F. Fried. *Phys. Rev. E*, **52**, 6227 (1995).
[40] V. Popa-Nita, T.J. Sluckin, A.A. Wheeler. *J. Phys. II, Paris*, **7**, 1225 (1997).
[41] A.K. Sen, D.E. Sullivan. *Phys. Rev. A*, **35**, 1391 (1987).
[42] A.D. Rey. *Macromol. Theory Simul.*, **4**, 857 (1995).
[43] S. Kumar. *Liquid Crystals in the Nineties and Beyond*. World Scientific, New Jersey (1995).
[44] C-H. Jang, L-L. Cheng, C.W. Olsen, N.L. Abbott. *Nano Lett.*, **6**, 1053 (2006).
[45] M.D. Lynch, D.L. Patrick. *Nano Lett.*, **2**, 1197 (2002).
[46] C. Lapointe, A. Hultgren, D.M. Silevitch, E.J. Felton, D.H. Reich, R.L. Leheny. *Science*, **303**, 652 (2004).
[47] P. Poulin, D.A. Weitz. *Phys. Rev. E*, **57**, 626 (1998).
[48] H.J. Coles. *Mol. Cryst. liq. Cryst.*, **49**, 67 (1978).
[49] R.D. Polak, G.P. Crawford, B.C. Kostival, J.W. Doane, S. Zumer. *Phys., Rev.* E, **49**, R978 (1994).
[50] R. Ondris-Crawford, G.P. Crawford, S. Zumer, J.W. Doane. *Phys. Rev. Lett.*, **70**, 194 (1993).
[51] J. Yan, A.D. Rey. *Phys. Rev. E.*, **65**, 031713 (2002).
[52] D.A. Dunmur, A. Fukuda, G.R. Luckhurst. *Physical Properties of Liquid Crystals: Nematics*. INSPEC, The Institute of Electrical Engineers, London (2001).
[53] A.J. Bray. *Adv. Phys.*, **51**, 481 (2002).
[54] G. De Luca, A.D. Rey. *Phys. Rev. E*, **69**, 011706 (2004).
[55] K. Skarp, S. Lagewall, B. Stebler. *Mol. Cryst. liq. Cryst.*, **60**, 215 (1980).
[56] A.D. Rey. *J. chem. Phys.*, **120**, 2010 (2004).
[57] A.D. Rey, M.M. Denn. *Annu. Rev. Fluid Mech.*, **34**, 233 (2002).
[58] A.D. Rey. *Mol. Cryst. liq. Cryst.*, **369**, 63 (2001).
[59] A.D. Rey. *J. chem. Phys.*, **113**, 10820 (2000).
[60] A.D. Rey. *Phys. Rev. E*, **61**, 1540 (2000).
[61] A.D. Rey. *Mol. Cryst. liq. Cryst.*, **338**, 197 (2000).
[62] A.D. Rey. *J. chem. Phys.*, **121**, 2390 (2004).
[63] A.D. Rey. *Phys. Rev. E*, **69**, 041707 (2004).
[64] A.D. Rey. *Phys. Rev. E*, **67**, 011706 (2003).
[65] A.D. Rey. *Liq. Cryst.*, **27**, 195 (2000).
[66] G.F. Mazenko. *Fluctuations, Order and Defects*. Wiley Interscience, HobokenNJ (2003).
[67] S. Chandrasekhar. *Liquid Crystals* second edn, Cambridge University Press, New York (1992).
[68] B. Wincure, A.D. Rey. *DCDS-B*, **8**, 623 (2007).
[69] O. Guzman, N.L. Abbott, J.J. de Pablo. *J. chem. Phys.*, **122**, 184711 (2005).